ACS OMEGA

http://pubs.acs.org/journal/acsodf

Article

Structure of Industrial Sacrificial Fragile Cementitious Foams

Shan Chen, Yang Zhao, Lang Jin, Qiang Zeng,* Zunpeng Huang, Ming Li, and Yajie Shi

Cite This: *ACS Omega* 2022, 7, 28493−28502

Read Online

ACCESS | Metrics & More | Article Recommendations | Supporting Information

ABSTRACT: Sacrificial fragile cementitious foams (SFCFs) act as a core material of the engineered material arresting system (EMAS) installed in airports to enhance the safe take-offs and landings of aircrafts. The foam structures and foaming mechanisms that greatly impact the collapse strength, specific energy, and arresting efficiency of SFCFs, however, have not been fully addressed. Herein, the engineering properties, chemical characteristics, and pore−skeleton structures of three batches of industrial SFCFs were experimentally investigated. Penetration tests showed significant differences in collapse strength and specific energy among the SFCFs with a similar density. Three-dimensional (3D) pore−skeleton structures were resolved by microfocused X-ray computed tomography. The pore−skeleton anisotropy was investigated to uncover the stages of differences in the SFCFs' engineering properties. The results demonstrate that the pore anisotropy rather than the porosity dominates the collapse of cementitious foams. Viscosity-associated nucleation and growth mechanisms were proposed to account for the featured pore−skeleton structures of the SFCFs. The findings would contribute to better pore structure controls of SFCFs toward the improved quality of EMAS.

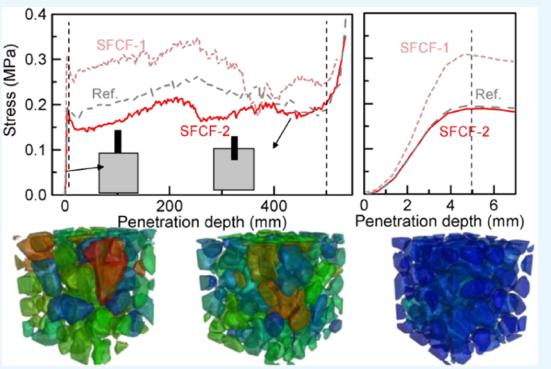

INTRODUCTION

The engineered material arresting system (EMAS) installed at the end of runways in airports is essential to reduce the risks of aircraft speeding out of the runway.[1,2] The core engineered materials in EMAS, which should involve the features of high energy absorption, reliability, and stability, must be sacrificed to prevent the crashing of an aircraft. As illustrated in Figure 1a, a Boeing 737 airplane was stopped in less than 300 m by an in situ arresting test of EMAS (Civil Aviation Administration of China (CAAC), Tianjin Binhai Int. Airport, Tianjin, China). At present, sacrificial fragile cementitious foams (SFCFs) may be a preferable material with the features of high energy absorption and low penetration resistance.[3,4] Generally, SFCF blocks are manufactured in a factory and then installed in situ according to the designs. Figure 1b shows the SFCF blocks that were readily prepared for installation, and Figure 1c shows the well-installed EMAS in Nyingchi Mainling Airport, Tibet, China. As a type of foamed composites with high collapse deformations under relatively low loads, most of the volume of SFCFs should be occupied by the air voids (over 80%), while the skeleton occupies the rest of the volume.[5−7] The porous structure of foam composites possesses some special properties, such as high thermal resistance, excellent sound absorption, and a high potential for energy storage, enabling wide applications in the energy system as well as in our daily life.[8−14]

It is generally accepted that the total porosity (identical to density if the material has stable chemical components) is the most decisive parameter to control the engineering performances of foam composites, and a higher total porosity leads to a lower strength.[15−17] Therefore, the quality of SFCF blocks for EMAS is often evaluated via foaming ratio (or density), as well as blocks' completeness (rated by the eyes). However, our practices during in situ industrial manufacturing of SFCF blocks indicated that the density and products' completeness as the product quality indexes are far from being sufficient for the quality controls of EMAS.[18] Neither the density nor the completeness can assess the structure of pores and skeletons. Moreover, to increase the skeleton's fragility, which would guarantee the material's sacrifice during loading, a large portion of the binding material (cement) in the skeleton is replaced with inert fillers like stone powder (SP).[19,20] The use of inert fillers in composite materials not only lowers the overall manufacturing costs but also alters the engineering performances of composites due to the complex microstructure and matrix−filler interactions.[21,22] The foam structure of SFCFs with inert fillers in EMAS may be altered, which, in turn, can impact the engineering performances of SFCFs. This thus provides strong incentives to clarify how foam structure impacts the engineering performances of SFCFs used in EMAS

Received: May 26, 2022
Accepted: July 27, 2022
Published: August 5, 2022

Figure 1. (a) Snapshot of a field test of EMAS arresting a Boeing 737 airplane in Tianjin Binhai Int. Airport by Civil Aviation Administration of China (CAAC). (b) SFCF blocks of EMAS unit ready for installation. (c) Picture of EMAS installed in the Nyingchi Mainling Airport, Tibet, China (photograph courtesy of Y.Z. Copyright 2022).

and to explore the foaming mechanisms that essentially govern the foam structure.

This work was also inspired by our practical observations that some batches of SFCF blocks showed a similar visual appearance and density but different engineering performances. We, therefore, hypothesized that the foam structure and chemical foaming mechanisms may play important roles in the final quality of SFCFs. Here, we selected three batches of in-situ-casted SFCFs from an EMAS manufacturer. The mechanical performances of the SFCF blocks were measured by a double-hole penetration (DhP) test. The microstructure and chemical characteristics of the SFCFs were investigated. Three-dimensional (3D) pores and skeletons, as well as the statistical structural parameters, were comprehensively investigated by micro-X-ray computed tomography (XCT), as it provides nondestructive tests with relatively large sample size and multiphase information.[23−25] Foaming mechanisms were proposed to sketch out how the foam-skeleton structures were formed. Our findings would deepen the understanding of foaming mechanisms and the associations between engineering properties and foam structure of SFCFs, which improve the quality controls during EMAS manufacturing.

MATERIALS AND METHODS

Materials. SFCF specimens were acquired from a local EMAS manufacturer (Hangke Technology Development Co., Ltd., Beijing, China). Three batches of SFCF blocks were produced in July 2019 and August 2019 (see Table 1 for the specific specimen information). The SFCF blocks from the first batch were adopted as the reference specimen as this batch belongs to a normal SFCF manufacturer. Two experimental batches were set with the changes in SP fillers. For the experimental batches, a type of PII.52.5 R cement (Conch, Anhui, China) was used as the only binding material. Melamine superplasticizer, $CaCl_2$ powder with a purity of >96.0%, and polypropylene fibers (6 mm in length and 15 μm in diameter) were purchased from local manufacturers to tune the workability and ductility of SFCF. Hydrogen peroxide (H_2O_2, at a concentration of 35%) and calcium stearate ($C_{36}H_{70}CaO_4$, purity >95%) purchased from Sinopharm Chemical Reagent, Tianjin, were used as the foaming agent and foam stabilizer, respectively.

Table 1. SFCF Specimens Used in this Work

SFCF batch date	specimen ID	quality control
July 13, 2019	SFCF-ref	density (≈0.2 kg/m^3), appearance (no obvious flaws)
August 03, 2019	SFCF-1	density (≈0.2 kg/m^3), appearance (no obvious flaws)
August 06, 2019	SFCF-2	density (≈0.2 kg/m^3), appearance (no obvious flaws)

Mineral components, micromorphology, and particle size distribution (PSD) of the solids were comprehensively characterized. Dolomite ($CaMg(CO_3)_2$) and calcite ($CaCO_3$) were the main minerals of all SPs (Figure S1), while a slight amount of brucite ($Mg(OH)_2$) was detected in SP-2 (Figure S2). The PSD of the fillers was tested using a laser particle size analyzer (LPSA, Beckman Coulter lS13320). The PSD curves of SP-1 and SP-2 were almost superimposed together at $D \leq 2$ μm (Figure 2). SP-1 showed lower PSD intensities but a greater upper limit than SP-2. Statistical analysis suggested that the characteristic sizes (mean size, median size, and D90) of SP-2 were lower than those of SP-1. The mean particle size of cement was 12.6 μm.

The micromorphology of the SPs was analyzed using a Phenom-World ProX Scanning Electron Microscopy (SEM) with an energy-dispersive X-ray spectrometer (EDX) (FOV: 53.7 μm, mode: 10 keV, image, detector: BSD full). SEM images showed that the SPs' particles all exhibited an irregular polyhedra morphology (Figures 3a and 4a). The element distribution of the local area of both SP samples was analyzed via EDX tests. For SP-1, O, C, Si, Mg, Te, and Ca are selectively shown in Figure 3b−g, where the Ca, Mg, and Te elements were present in most areas of the selected zone. For SP-2, similar elements were detected, except that Al replaced

https://doi.org/10.1021/acsomega.2c03283
ACS Omega 2022, 7, 28493−28502

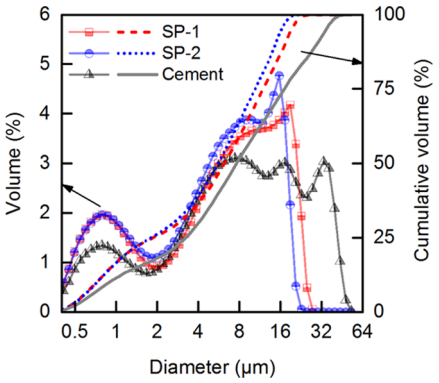

Figure 2. Differential and accumulative PSD curves of SP-1, SP-2, and cement.

Te (Figure 4b–g). The slenderness of SP-1 particles appeared to be higher than that of SP-2 (Figures 3a and 4a).

Industrial SFCF Manufacturing. SFCF blocks were fabricated in a local concrete factory (Tianjin, China) according to the standardized processes with the predesigned material proportions (Table S1). The system of material supply, mixing, and molding was integrated into a three-floor frame (Figure 5a). The processes can be summarized as follows. First, the dry raw materials, including cement, filler, and additives, were pumped from the material containers according to the mix proportions (Figure 5b). After a short dry mixing stage (30 s), water was added for primary wet mixing with the stirring rate of 120 r/min for 3 min (Figure 5c). Then, hydrogen peroxide solution was added to the cementitious slurries with a high stirring speed of 200 r/min for 10 s. The homogeneously mixed slurries were then cast into large molds (Figure 5d). Once the foaming was completed, SFCF blocks, together with the molds, were carefully moved into a chamber for the primary curing (temperature between 32 and 34 °C, humidity over 95%). After 24 h, the molds were removed, and the blocks were stored in a natural curing room until the set aged.

Test Methods. Each batch of SFCF blocks experienced comprehensive in-lab physical and mechanical tests. Representative blocks were cut from each huge SFCF unit (1000 × 1000 × 500 mm^3) for specific tests. A homemade DhP testing scheme was applied to test the mechanical behaviors of a large SFCF unit. This testing scheme may approach the materials crashing under loads of aircraft tires.[18] The forces and displacements of each cube were recorded with a DNS-20 testing machine equipped with a penetration rod of 50.8 mm in diameter.

Central cubic blocks with an edge length of 100 mm were acquired for density measurement. A gravity method that records the weight and volume of the sample, and calculates their ratio, was used. Six replicas were conducted to enhance the data reliability.

The micromorphology of the hardened SFCF blocks was observed via an SEM (FEI Quanta FEG650) with an accelerating voltage of 20 keV and a spot size of 4.

Crystal minerals of the SFCF samples were tested by X-ray diffraction (XRD) using a Bruker D8 Advance diffractometer with Cu Kα radiation ($\lambda = 0.15419$ nm) in a continuous scanning pattern between 5 and 90° and a step length of 0.02°. MDI Jade 6 was used for mineral phase identification.

Chemical bonds of the SFCFs were tested by Fourier transform infrared spectroscopy (FTIR, Nicolet iS50) in a wavenumber range of 4000 and 400 cm^{-1} with a spectral resolution of 4 cm^{-1} and a set of 32 scans. Before each FTIR test, sample-free FTIR scans were first performed to filtrate the background noises.

Thermogravimetry–derivative thermogravimetry (TG–DTG) tests were conducted using a thermal analyzer thermal gravimetric analysis (TGA) (Mettler Toledo Corp., Switzerland) with the temperature increasing at a rate of 10 °C/min up to 1000 °C in a nitrogen atmosphere.

Cubic samples with a side length of 50 mm were acquired from the central part of each SFCF unit (Figure 6a,b) and used for the pore structure test by micro-X-ray computed tomography (micro-XCT, XTH255/320 LC, Nikon, Japan). An SFCF sample was first fixed on the sample frame between the X-ray beams delivered and a high-resolution detector (2000 × 2000 pixels) (Figure 6c). As the sample frame rotated evenly by 360° in 1500 s, X-ray beams at an accelerating voltage of 160 kV and the beam current of 120 μA penetrated through the SFCF sample, and the detector recorded the transmission projection at the same time (Figure 6d). A total of 2001 projections of each SFCF sample were loaded into a CT Pro software for generating numerous gray images with a resolution of 43 μm/pixel. These images were imported into VG Studio MAX 3.1 software for pore and skeleton analyses (Figure 6e). A region of interest (ROI) with a side length of 25

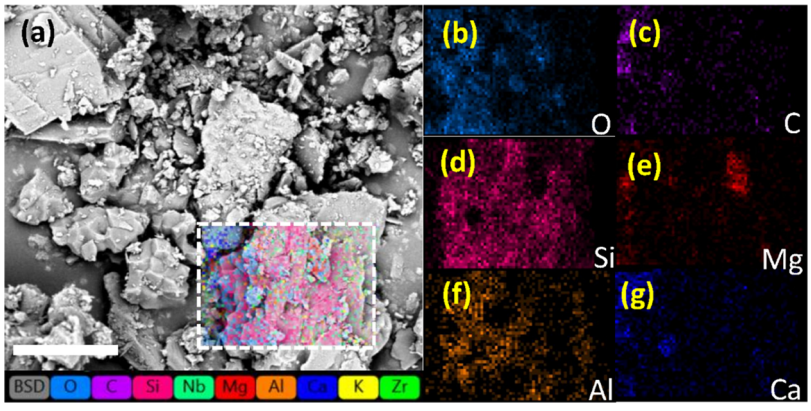

Figure 3. (a) Micromorphology of SP-1 and the element mapping of (b) O, (c) C, (d) Si, (e) Mg, (f) Te, and (g) Ca in a local area (scale bar = 10 μm).

https://doi.org/10.1021/acsomega.2c03283
ACS Omega 2022, 7, 28493–28502

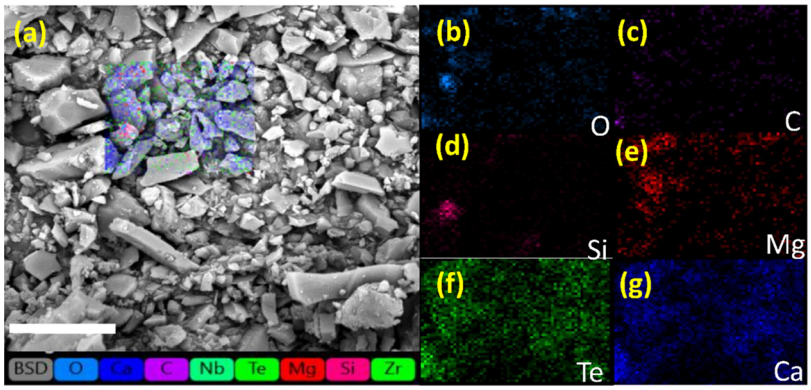

Figure 4. (a) Micromorphology of SP-2 and the element mapping of (b) O, (c) C, (d) Si, (e) Mg, (f) Al, and (g) Ca in a local area (scale bar = 10 μm).

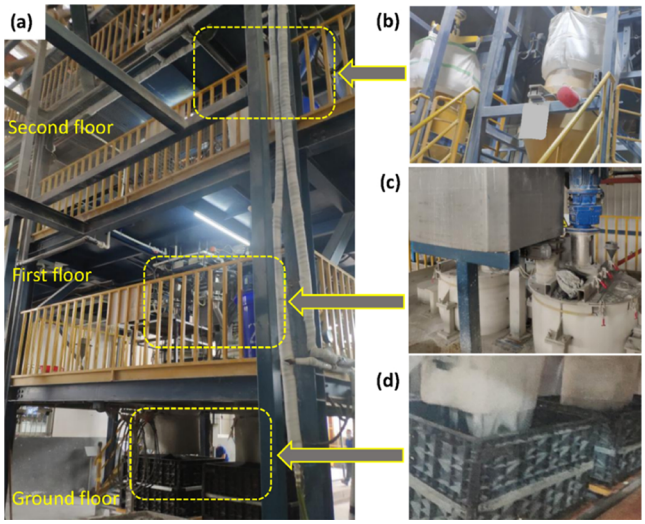

Figure 5. Manufacturing processes of SFCF: (a) a multifloor frame with the raw materials in the second floor, mixing machine in the first floor, and molds in the ground floor; (b) chambers for the raw materials; (c) the electric mixing device; and (d) an in situ picture of SFCF casting (photograph courtesy of Y.Z. Copyright 2022).

mm was selected from each SFCF specimen for elaborate 3D structural analysis (Figure 6f).

RESULTS AND DISCUSSION

Mechanical Properties. Typical strength−depth curves of SFCF-1, SFCF-2, and SFCF-ref are shown in Figure 7a. For all SFCF cubes, the stress−depth curves can be divided into three zones: (a) the short, linear, and rapid stress-rising zone with limited deformation due to the elastic deformation; (b) the long, nonlinear, and strength-fluctuation zone due to the continuous collapses of foams during penetration; and (c), the moderate, nonlinear, and rapid stress-rising zone due to the material compaction and densification under the indenter. The elastic stage was rapidly completed as the penetration displacement arrived at 5 mm for all SFCFs (Figure 7b). After that, the foams collapsed to sustain the external penetration. For foams with ideally homogeneous distribution and isotropic geometry, the continual collapse of the foams would yield a relative plate stress stage. However, due to the heterogeneity and anisotropy of the foams, the external stresses were fluctuated for a relatively long range.[18] Large stress drops from 0.3 to 0.2 MPa at the penetration depths of 350−400 mm

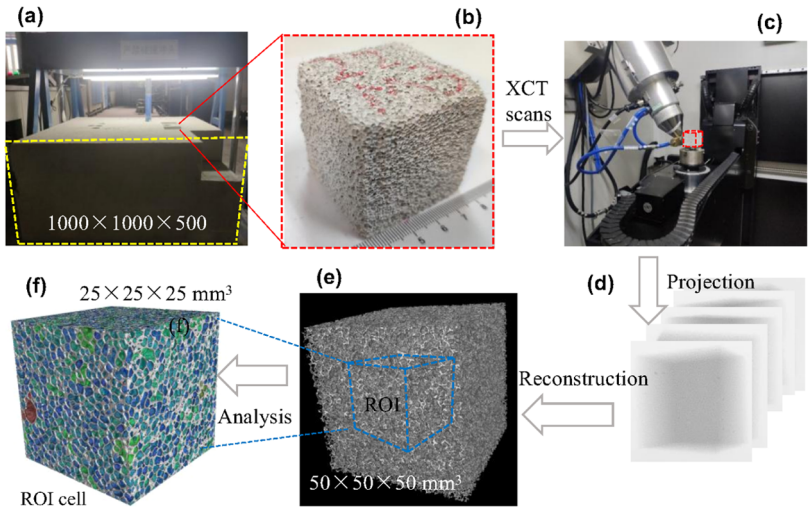

Figure 6. XCT test and analysis procedures: (a) a demolded huge SFCF block with the dimensions of 1000 × 1000 × 500 mm^3 (photograph courtesy of Y.Z. Copyright 2022); (b) a selected small SFCF cube with the dimensions of 50 × 50 × 50 mm^3 after cutting for the XCT test; (c) an in situ picture of XCT scans; (d) selected displays of X-ray attenuation projections of the sample; (e) 3D model reconstructed skeleton structure; and (f) pore−skeleton structure after data analysis on the cube region of interest (ROI).

https://doi.org/10.1021/acsomega.2c03283
ACS Omega 2022, 7, 28493−28502

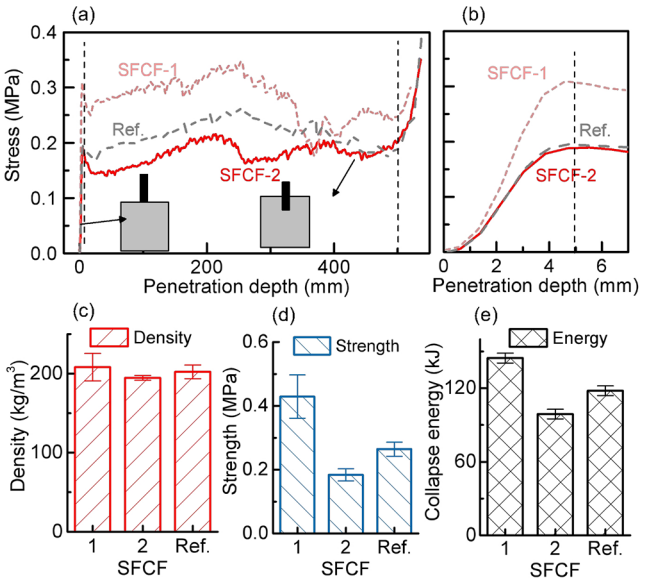

Figure 7. Mechanical and physical properties of three SFCFs: (a) representative stress−depth curves by the DhP test and (b) the magnified elastic stage of stress−depth curves; statistics results of (c) density, (d) strength, and (e) collapse energy.

were observed for SCFC-1 owing to the presence of structural heterogeneity of the foams (Figure 7a). The length of each zone showed no differences among the SFCFs, suggesting that they possessed a similar foaming rate.

Density tests indicated that all SFCFs showed similar densities, that is, ρ(SFCF-1) = 206.2 kg/m^3, ρ(SFCF-2) = 194.6 kg/m^3, and ρ(Ref) = 202.2 kg/m^3 (Figure 7c). The average stresses in the middle collapse zone (penetration depth of 50−500 mm) were adopted as the SFCFs' collapse strength. As demonstrated in Figure 7d, compared with the ref SFCF specimens (0.264 MPa), the average collapse strength of SFCF-1 was dramatically increased to 0.426 MPa by 61.4%, while that of SFCF-2 showed moderate strength decreases to 0.184 MPa by 30.3% (Figure 7d). The specific collapse energy, which can be consumed to counteract the energy of motion of an airplane, was evaluated by integrating the stress−depth curves up to 500 mm. The collapse energy of SFCF-ref of 118.0 kJ/m^2 was substantially lower than that of SFCF-1 (144.6 kJ/m^2) by 22.5%, but greatly higher than that of SFCF-2 (98.9 kJ/m^2) by 19% (Figure 7e). The data demonstrated that SFCFs with a similar density had great differences in collapse strength and energy.

Chemical Test Outcomes. Chemical testing results of XRD, FTIR, and TG−DTG are shown in Figure 8. In XRD patterns, the characteristic peaks of dolomite, calcite, quartz, portlandite, and brucite were recognized in the SFCFs (Figure 8a). Except for the portlandite that was generated from the cement hydration, the other minerals mainly came from the SPs (Figure S2). Carbonation may occur in the portlandite in the SFCF-ref sample, and so a higher intensity of calcite was observed (Figure 8a). For FTIR tests, very similar FTIR spectra between SFCF-1 and SFCF-2 were observed (Figure 8b). The minerals in the fillers (e.g., dolomite and calcite) accounted for the superposed characteristic FTIR peaks between the SFCF and SP samples, while the cement hydration products accounted for the rest of the characteristic FTIR peaks (Figure 8b). For TG−DTG tests, three mass loss peaks were identified (Figure 8c): the loss of bound water and/or the decomposition of ettringite below 200 °C,[26,27] the decomposition of portlandite and/or brucite between 300 and 500 °C, and the decomposition of dolomite and/or calcite between 650 and 800 °C.[28,29] As demonstrated in Figure 8c, around 29% mass loss of the third peak was estimated for SFCF-ref, and 25 and 22% were observed for SFCF-1 and SFCF-2, respectively (Figure 8c). The results of TG−DTG are consistent with those of XRD. The highest content of calcite in SFCF-ref may partially account for the highest strength (Figure 7a,c) as calcite generally has a higher mechanical strength than cement hydrates.

For SEM analysis, the magnifications of 100× to 200× were first chosen to observe the macromorphology of the pores and

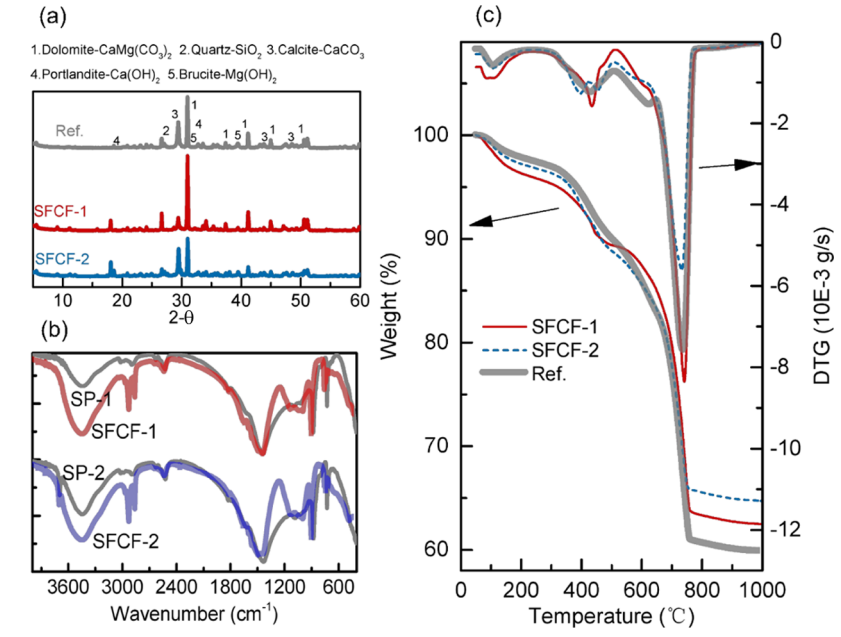

Figure 8. Chemical test outcomes: (a) XRD patterns, (b) FTIR spectra, and (c) TG−DTG curves.

https://doi.org/10.1021/acsomega.2c03283
ACS Omega 2022, 7, 28493−28502

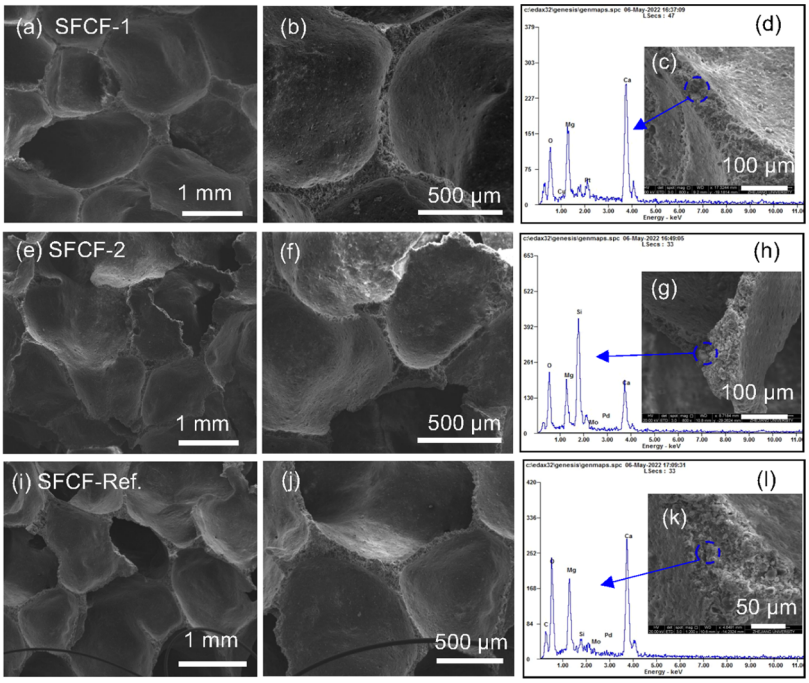

Figure 9. SEM-EDX results of (a–d) SFCF-1, (e–h) SFCF-2, and (i–l) SFCF-ref: (a, e, i) foam and skeleton morphology; (b, f, j) pore wall morphology; (c, g, k) morphology of the fractured skeletons; and (d, h, l) EDX spectra of local sites in the skeletons.

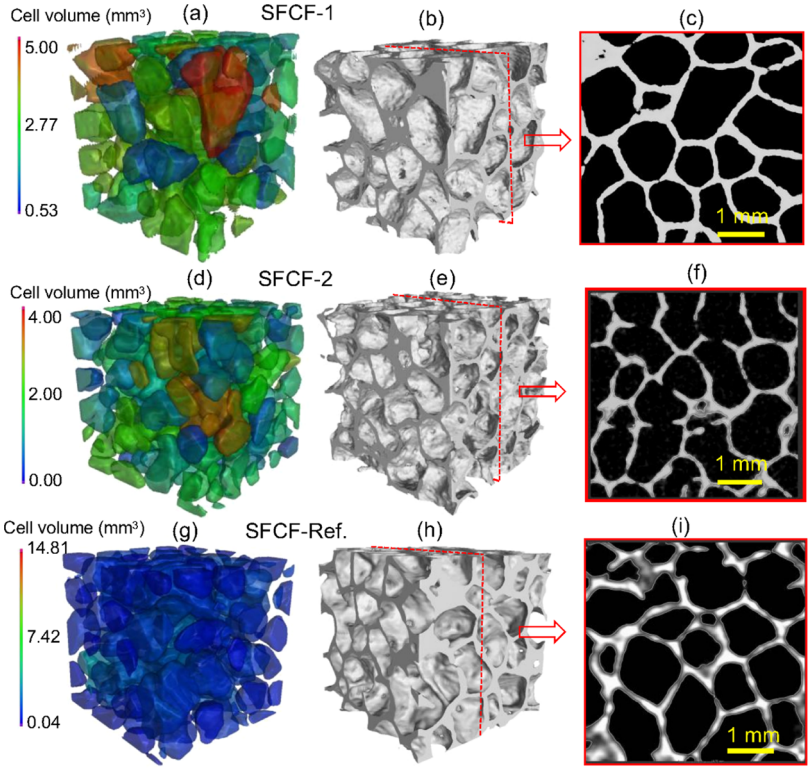

Figure 10. Pore and skeleton structures from micro-XCT: 3D structure of pores (a, d, g) and skeletons (b, e, h); selected 2D slices (c, f, i).

skeletons (Figure 9a,e,i). It seems that SFCF-1 had a larger pore size and smoother pore walls than SFCF-2 and SFCF-ref (Figure 9b,f,j). On the contrary, SFCF-2 showed tortuous skeletons (Figure 9e,f). When the fracture surface of the skeletons in SFCFs was focused on, relatively tight compaction of the cement hydrates and SP particles was observed for all samples (Figure 9c,g,k). EDX tests on local SP particles confirmed the greatest peak intensity of silicon in SFCF-1 (Figure 9h), indicating the highest content of quartz in the SP, in line with the data of XRD (Figure 8a). For SFCF-ref and SFCF-2, a great amount of calcium was detected (Figure 9d,i), indicating the high content of dolomite and calcite.

Foam Structure. Foam structure was resolved by micro-XCT to unravel the mechanisms of strength difference beyond

https://doi.org/10.1021/acsomega.2c03283
ACS Omega 2022, 7, 28493−28502

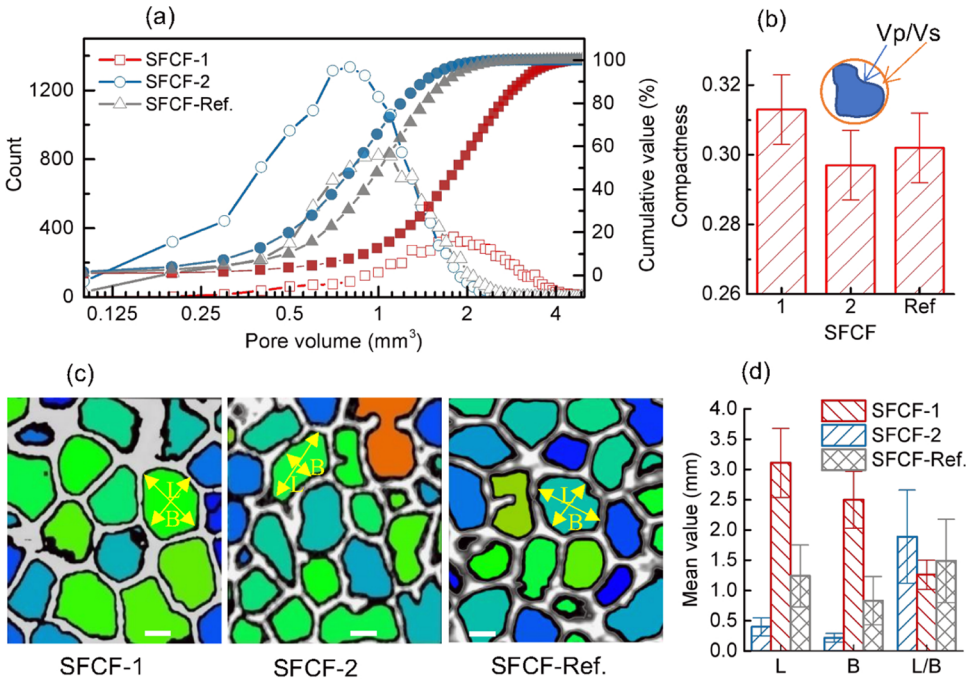

Figure 11. (a) Pore volume distributions of the SFCFs and (b) compactness; (c) 2D illustrations of selected sections (scale bar = 0.6 mm), and (d) statistical results of length (L), width (B), and the aspect ratio (L/B).

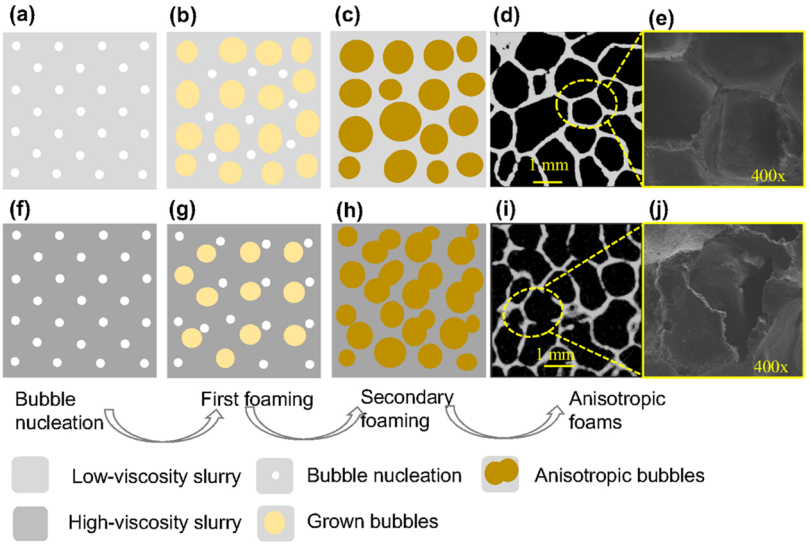

Figure 12. Viscosity-governed foaming mechanisms for SFCFs with low-viscosity slurry (a–e) and high viscosity slurry (f–j): foaming nucleation (a, f), growth (b, g), secondary foaming around the old bubbles (c, h), micro-XCT images of skeletons (d, i), and SEM images of foam structures (e, j).

the issues of material component and morphology. Typical analysis results of micro-XCT are demonstrated in Figure 10. At a first glance, SFCF-1 had larger pores (Figure 10a,d,g) and thicker pore walls (Figure 10b,e,h) than SFCF-2 and SFCF-ref. The 2D sectional images implied that the pore walls of SFCF-1 were mostly connected to form continuous skeletons, while a large portion of the pore walls of SFCF-2 was broken, and the skeletons were rather tortuous (Figure 10c,f,i). The completeness and continuity of SFCF-ref were between those of SFCF-1 and SFCF-2.

Pore volume distribution (PVD) and compactness were statistically analyzed based on a cubic ROI of 25 mm in length. Roughly, all PVD spectra followed the lognormal distribution that was extensively reported to capture the distributions of pores in cement pastes and rocks.[30,31] Compared with SFCF-2 and SFCF-ref, SFCF-1 showed a much wider pore size range and weaker PVD intensity. Within the same ROI volume, the pore number order was SFCF-2 > SFCF-ref > SFCF-1, while the most probably distributed pore size (the size at the peak intensity of PVD spectra) possessed the opposite order (Figure 11a). Specifically, the PVD peak size was roughly 2 mm for SFCF-1, 1 mm for SFCF-ref, and 0.7 mm for SFCF-2. The anisotropy of those pores in the ROI for each SFCF was characterized by pore compactness, which is defined as the volume ratio between a pore (V_p) and the circumscribed sphere (V_s) (Figure 11b). The compactness with the typical

https://doi.org/10.1021/acsomega.2c03283
ACS Omega 2022, 7, 28493−28502

value between 0 and 1 measures the deviation extents of a pore from an ideal sphere. The closer the compactness to 1, the lower the deviation of the pore from the ideal spheres.[32] The pore compactness values of all SFCFs were relatively small (~0.3), suggesting the high anisotropy of the foams. Analysis in detail indicated that the pore compactness of SFCF-1 was the highest (0.313), that of SFCF-2 was the lowest (0.297), and that of SFCF-ref was between those of SFCF-1 and SFCF-2 (0.302) (Figure 11b). A material with a higher pore anisotropy generally has a lower strength. In this sense, the greater pore anisotropy may partially account for the lower collapse strength for the SFCFs tested.

Statistical analysis of the selected pores yielded a much higher pore length (L) and width (B) but a lower aspect ratio (L/B) in SFCF-1 (Figure 11c), suggesting that the pores of SFCF-1 were closer to the sphere and more isotropic when compared with those of SFCF-2 and SFCF-ref. The lower pore anisotropy (Figure 11d) and skeleton tortuosity of SFCF-1 (Figure 10c) may account for the higher strength (Figure 7d). Such pore−skeleton structural mechanisms were also employed to tune the macroproperties of composites in different application scenarios.[33,34]

Discussion on Foaming Mechanisms. In this work, all of the SFCFs possessed completely the same manufacturing processes; however, a largely different collapse strength and pore−skeleton structure was reported (Figures 7, 9−11). Foaming mechanisms may be essential to address the experimental outcomes. The foaming processes of cementitious composites and other foamed materials are intimately related to the slurries' viscosity that can be affected by the particle size, morphology, and other characteristics of the materials.[33,35−38] In our work, different particle size distributions and particle morphology were observed for the fillers (Figures 2−4), which would cause different viscosities of the cementitious slurries with the same mix proportions. At the beginning stage of foaming, H_2O_2 decomposed into water and oxygen, and bubbles would homogeneously nucleate in the slurries (Figure 12a,f). When larger fillers (for instance, SP-1) were added to cement, the slurries' viscosity would be lower,[39−41] facilitating the growth of bubbles and secondary nucleation (Figure 12b,c). In this case, after the material was hardened, relatively isotropic and homogeneous voids and skeletons (Figure 12d,e) formed a foam structure with relatively high strength (SFCF-1). However, for the slurries with higher viscosity due to the addition of thinner fillers (for instance, SP-2), the foaming resistance was higher,[42] and bubbles, therefore, grew slower and smaller (Figure 12g). Meanwhile, the foaming resistance around the already formed bubbles decreased, and so new bubbles were more likely to nucleate in the vicinity of the old bubbles and penetrate through the pore walls (Figure 12g,h). In this heterogeneous foaming regime, anisotropic voids and tortuous skeletons formed a more complex foam structure (Figure 12i,j) with a relatively lower strength (SFCF-2). This viscosity-governed foaming mechanism may also partially account for the structural differences of SFCFs cast under different temperatures.[18]

Overall, our tests demonstrated that the industrially manufactured SFCFs can possess different engineering performances in terms of collapse strength and specific arresting energy even though they have similar density values. If we only adopted density, which may be the easiest way for measurement, as the only index to screen the quality of SFCF, the final EMAS may not serve well to arrest the aircraft when running off the runway. Our work explored the pore−skeleton anisotropy that may greatly impact the engineering performances and the foaming mechanisms that govern the pore−skeleton structure. It is, therefore, crucial to set more indexes other than density, foaming rate, and visual ratings by the eyes, such as slurries' property controls and pore structure measurement, to improve the quality controls of EMAS for safer airports.

CONCLUSIONS

Three batches of industrial SFCFs for EMAS with the same manufacturing processes possessed similar density values but different collapse strengths and specific energy. The SPs used influenced the patterns of XRD, FTIR, and TGA due to their intrinsic minerals but had minor impacts on cement hydration products. SEM and micro-XCT tests demonstrated that SFCF-1 had the weakest PVD intensity, largest pore size, highest compactness, and lowest pore aspect ratio. The lowest pore anisotropy and skeleton tortuosity of SFCF-1 accounted for the largest collapse strength and specific energy. Different foam structures were ascribed to the nucleation and growth of foams in slurries with different viscosities. The findings not only deepen the viscosity-associated nucleation and growth of foams in slurries but also enable improving SFCF quality controls toward more stable EMAS and safer airports.

ASSOCIATED CONTENT

Supporting Information

The Supporting Information is available free of charge at https://pubs.acs.org/doi/10.1021/acsomega.2c03283.

Characterizations of natural SPs; testing details; manufacturing processes; pore parameters, and SEM-EDX data of the SFCF samples (PDF)

AUTHOR INFORMATION

Corresponding Author

Qiang Zeng − *College of Civil Engineering and Architecture, Zhejiang University, Hangzhou 310058, P. R. China;* orcid.org/0000-0003-1720-4766; Email: cengq14@zju.edu.cn

Authors

Shan Chen − *College of Civil Engineering and Architecture, Zhejiang University, Hangzhou 310058, P. R. China*

Yang Zhao − *Engineering and Technical Research Center of Civil Aviation Safety Analysis and Prevention, China Academy of Civil Aviation Science and Technology, Beijing 100028, P. R. China*

Lang Jin − *Hangke Technology Development Co., Ltd., China Academy of Civil Aviation Science and Technology, Beijing 100028, P. R. China*

Zunpeng Huang − *China Academy of Civil Aviation Science and Technology, Beijing 100028, P. R. China*

Ming Li − *China Academy of Civil Aviation Science and Technology, Beijing 100028, P. R. China*

Yajie Shi − *Engineering and Technical Research Center of Civil Aviation Safety Analysis and Prevention, China Academy of Civil Aviation Science and Technology, Beijing 100028, P. R. China*

Complete contact information is available at: https://pubs.acs.org/10.1021/acsomega.2c03283

https://doi.org/10.1021/acsomega.2c03283
ACS Omega 2022, 7, 28493−28502

Funding

The research was supported by the National Key R&D Program of China (No. 2017YFB0309903) and The Open Project Fund 2019 of Engineering and Technical Research Center of Civil Aviation Safety Analysis and Prevention of Beijing.

Notes

The authors declare no competing financial interest.

■ ACKNOWLEDGMENTS

The authors thank Yu Peng from the Experimental Center of CCEA, Zhejiang University, for the technical assistance with XCT tests.

■ REFERENCES

(1) Yang, X.; Yang, J.; Zhang, Z.; Ma, J.; Sun, Y.; Liu, H. A Review of Civil Aircraft Arresting System for Runway Overruns. *Prog. Aerosp. Sci.* **2018**, *102*, 99−121.

(2) Xing, Y.; Yang, X. F.; Yang, J. L.; Sun, Y. X. A Theoretical Model of Honeycomb Material Arresting System for Aircrafts. *Appl. Math. Modell.* **2017**, *48*, 316−337.

(3) Yang, X. F.; Zhang, Z. Q.; Xing, Y.; Yang, J. L.; Sun, Y. X. A New Theoretical Model of Aircraft Arresting System Based on Polymeric Foam Material. *Aerosp. Sci. Technol.* **2017**, *66*, 284−293.

(4) Steyn, W. J.; Lombard, S.; Horak, E. Foamed Concrete-Based Material as a Soft Ground Arresting System for Runways and Airfields. *J. Perform. Constr. Facil.* **2016**, *30*, No. C4014006.

(5) Minas, C.; Carpenter, J.; Freitag, J.; Landrou, G.; Tervoort, E.; Habert, G.; Studart, A. R. Foaming of Recyclable Clays into Energy-Efficient Low-Cost Thermal Insulators. *ACS Sustainable Chem. Eng.* **2019**, *7*, 15597−15606.

(6) Qian, W.; Zhao, K.; Zhang, D.; Bowen, C. R.; Wang, Y.; Yang, Y. Piezoelectric Material-Polymer Composite Porous Foam for Efficient Dye Degradation via the Piezo-Catalytic Effect. *ACS Appl. Mater. Interfaces* **2019**, *11*, 27862−27869.

(7) Chen, Y.; Huang, X.; Zhang, S.; Li, S.; Cao, S.; Pei, X.; Zhou, J.; Feng, X.; Wang, B. Shaping of Metal−Organic Frameworks: From Fluid to Shaped Bodies and Robust Foams. *J. Am. Chem. Soc.* **2016**, *138*, 10810−10813.

(8) Zhang, X.; Wu, G.; Yang, X. MoS2 Nanosheet−Carbon Foam Composites for Solar Steam Generation. *ACS Appl. Nano Mater.* **2020**, *3*, 9706−9714.

(9) Zhu, J.; Sakaushi, K.; Clavel, G.; Shalom, M.; Antonietti, M.; Fellinger, T. A General Salt-Templating Method To Fabricate Vertically Aligned Graphitic Carbon Nanosheets and Their Metal Carbide Hybrids for Superior Lithium Ion Batteries and Water Splitting. *J. Am. Chem. Soc.* **2015**, *137*, 5480−5485.

(10) Jiang, J.; Feng, W.; Zhao, D.; Zhai, W. Poly(ether imide)/Epoxy Foam Composites with a Microcellular Structure and Ultralow Density: Bead Foam Fabrication, Compression Molding, Mechanical Properties, Thermal Stability, and Flame-Retardant Properties. *ACS Omega* **2020**, *5*, 25784−25797.

(11) Xiao, X.; Jia, H.; Pervaiz, S.; Wen, D. Molten Salt/Metal Foam/Graphene Nanoparticle Phase Change Composites for Thermal Energy Storage. *ACS Appl. Nano Mater.* **2020**, *3*, 5240−5251.

(12) Oh, J.-H.; Kim, J.; Lee, H.; Kang, Y.; Oh, I. Directionally Antagonistic Graphene Oxide-Polyurethane Hybrid Aerogel as a Sound Absorber. *ACS Appl. Mater. Interfaces* **2018**, *10*, 22650−22660.

(13) Wei, L. S.; Zuo, W. Q.; Pan, H.; Lyu, K.; Zhang, W. H.; She, W. Rational Design of Lightweight Cementitious Composites with Reinforced Mechanical Property and Thermal Insulation: Particle Packing, Hot Pressing Method, and Microstructural Mechanisms. *Composites, Part B* **2021**, *226*, No. 109333.

(14) Tiwari, S. K.; Chen, D.; Chen, Y.; Thummavichai, K.; Ola, O.; Ma, Z.; Liu, G.; Wang, N.; Zhu, Y. N-Doped Graphenelike Nanostructures from p-Nitro Aniline-Based Foam: Formation, Structure, and Applications as a Nanofiller. *ACS Omega* **2022**, *7*, 3230−3239.

(15) Kapat, K.; Srivas, P. K.; Rameshbabu, A. P.; Maity, P. P.; Jana, S.; Dutta, J.; Majumdar, P.; Chakrabarti, D.; Dhara, S. Influence of Porosity and Pore-Size Distribution in Ti6Al4 V Foam on Physicomechanical Properties, Osteogenesis, and Quantitative Validation of Bone Ingrowth by Micro-Computed Tomography. *ACS Appl. Mater. Interfaces* **2017**, *9*, 39235−39248.

(16) Ge, Z.; Chen, H.; Ren, Y.; Xiao, P.; Yang, Y.; Zhang, T.; Ma, Y.; Chen, Y. A Universal Method for the Preparation of Dual Network Reduced Graphene Oxide−Ceramic/Metal Foam Materials with Tunable Porosity and Improved Conductivity. *Chem. Mater.* **2018**, *30*, 8368−8374.

(17) Yang, C.; Chen, F.; Sun, J.; Chen, N. Boosted Mechanical Piezoelectric Energy Harvesting of Polyvinylidene Fluoride/Barium Titanate Composite Porous Foam Based on Three-Dimensional Printing and Foaming Technology. *ACS Omega* **2021**, *6*, 30769−30778.

(18) Jin, L.; Chen, S.; Zhao, Y.; Zeng, Q.; Huang, Z.; Li, M.; Shi, Y. Characterizing The Foam-shell Microstructure of Industrial Ultra-light Foamed Concrete Cast under Different Temperatures. *Mater. Charact.* **2021**, *173*, No. 110938.

(19) Li, C.; Wu, M.; Yao, W. Eco-efficient Cementitious System Consisting of Belite-Ye'elimite-Ferrite Cement, Limestone Filler, and Silica Fume. *ACS Sustainable Chem. Eng.* **2019**, *7*, 7941−7950.

(20) Ketov, A.; Rudakova, L.; Vaisman, I.; Ketov, I.; Haritonovs, V.; Sahmenko, G. Recycling of Rice Husks Ash for The Preparation of Resistant, Lightweight and Environment-friendly Fired Bricks. *Constr. Build. Mater.* **2021**, *302*, No. 124385.

(21) Colangelo, F.; Roviello, G.; Ricciotti, L.; Ferrándiz-Mas, V.; Messina, F.; Ferone, C.; Tarallo, O.; Cioffi, R.; Cheeseman, C. R. Mechanical and Thermal Properties of Lightweight Geopolymer Composites. *Cem. Concr. Compos.* **2018**, *86*, 266−272.

(22) Doan, T. T. L.; Brodowsky, H. M.; Gohs, U.; Mäder, E. Re-Use of Marble Stone Powders in Producing Unsaturated Polyester Composites. *Adv. Eng. Mater.* **2018**, *20*, No. 1701061.

(23) Chang, B.; Du, C.; Sun, M.; Lin, Y.; Wang, Y.; Chu, X.; Zhang, L.; He, J. Mesoscopic Seepage Simulation and Analysis of Unclassified Tailings Pores Based on 3D Reconstruction Technology. *ACS Omega* **2021**, *6*, 14309−14316.

(24) Panduro, E. A. C.; Torsæter, M.; Gawel, K.; Bjørge, R.; Gibaud, A.; Yang, Y.; Bruns, S.; Zheng, Y.; Sørensen, H. O.; Breiby, D. W. In-Situ X-ray Tomography Study of Cement Exposed to CO_2 Saturated Brine. *Environ. Sci. Technol.* **2017**, *51*, 9344−9351.

(25) Tsvirkun, D.; Ben-Nun, Y.; Merquiol, E.; Zlotver, I.; Meir, K.; Weiss-Sadan, T.; Matok, I.; Popovtzer, R.; Blum, G. CT Imaging of Enzymatic Activity in Cancer Using Covalent Probes Reveal a Size-Dependent Pattern. *J. Am. Chem. Soc.* **2018**, *140*, 12010−12020.

(26) Zhang, Y.; Zhao, Q.; Gao, Z.; Chang, J. Microstructure Control of AH3 Gel Formed in Various Calcium Sulfoaluminate Cements as a Function of pH. *ACS Sustainable Chem. Eng.* **2021**, *9*, 11534−11547.

(27) Yan, D.; Lu, J.; Sun, Y.; Wang, T.; Meng, T.; Zeng, Q.; Liu, Y. CO2 Pretreatment to Aerated Concrete with High-Volume Industry Wastes Enables a Sustainable Precast Concrete Industry. *ACS Sustainable Chem. Eng.* **2021**, *9*, 3363−3375.

(28) Martins, F. M.; Martins, J. M.; Ferracin, L. C.; da Cunha, C. J. Mineral Phases of Green Liquor Dregs, Slaker Grits, Lime Mud and Wood Ash of a Kraft Pulp and Paper Mill. *J. Hazard. Mater.* **2007**, *147*, 610−617.

(29) Ariskina, K. A.; Abaas, M.; Yuan, C. D.; Emelianov, D. A.; Varfolomeev, M. A. Effect of Calcite and Dolomite on Crude Oil Combustion Characterized by TG-FTIR. *J. Pet. Sci. Eng.* **2020**, *184*, No. 106550.

(30) Zeng, Q.; Li, L.; Pang, X.; Gui, Q.; Li, K. Freeze-thaw Behavior of Air Entrained Cement Paste Saturated with 10 wt. % NaCl Solution. *Cold Reg. Sci. Technol.* **2014**, *102*, 21−31.

(31) Berthonneau, J.; Grauby, O.; Jolivet, I. C.; Gelin, F.; Chanut, N.; Magnin, Y.; Pellenq, R. J.-M.; Ferry, D. Nanoscale Accessible

https://doi.org/10.1021/acsomega.2c03283
ACS Omega 2022, 7, 28493−28502

Porosity as a Key Parameter Depicting the Topological Evolution of Organic Porous Networks. *Langmuir* **2021**, *37*, 5464−5474.
(32) Peng, Y.; Zhao, G.; Qi, Y.; Zeng, Q. In-situ Assessment of the Water-penetration Resistance of Polymer Modified Cement Mortars by μ-XCT, SEM and EDS. *Cem. Concr. Compos.* **2020**, *114*, No. 103821.
(33) Yeetsorn, R.; Tungkamani, S.; Maiket, Y. Fabrication of a Ceramic Foam Catalyst Using Polymer Foam Scrap via the Replica Technique for Dry Reforming. *ACS Omega* **2022**, *7*, 4202−4213.
(34) Li, Y.; Liu, J.; Deng, Y.; Han, X.; Hu, W.; Zhong, C. Finite-Element Analysis on Percolation Performance of Foam Zinc. *ACS Omega* **2018**, *3*, 11018−11025.
(35) Wang, X.; Chen, H.; Zhao, L.; He, X.; Fang, W.; Li, W. Relation between Rheological and Curing Behavior of Inorganic Foam Slurries in the Gel-Casting Process. *Ind. Eng. Chem. Res.* **2018**, *57*, 4261−4267.
(36) Luo, Y.; Ni, L.; Yan, L.; Zou, H.; Zhou, S.; Liang, M. Structure to Properties Relations of Polyimide Foams Derived from Various Dianhydride Components. *Ind. Eng. Chem. Res.* **2021**, *60*, 9489−9499.
(37) Shi, B.-H.; Chai, S.; Wang, L.; Lv, X.; Liu, H.; Wu, H.; Wang, W.; Yu, D.; Gong, J. Viscosity Investigation of Natural Gas Hydrate Slurries with Anti-agglomerants Additives. *Fuel* **2016**, *185*, 323−338.
(38) Liu, Y.; Meng, Z.; Wang, Y.; Li, P.; Sun, Y. Analysis and Modeling of Viscosity for Aqueous Polyurethane Dispersion as a Function of Shear Rate, Temperature, and Solid Content. *ACS Omega* **2020**, *5*, 26237−26244.
(39) Liu, R.; Zhang, C.; Pei, Y.; Chen, M.; Liu, H.; Li, X. Influence of Flocculation Effect on the Apparent Viscosity of Cement Slurry and Analysis of Different Influencing Factors. *Constr. Build. Mater.* **2021**, *281*, No. 122602.
(40) Liu, P.; Zhu, M.; Zhang, Z.; Leong, Y.; Zhang, Y.; Zhang, D. Rheological Behaviour and Stability Characteristics of Biochar-water Slurry Fuels: Effect of Biochar Particle Size and Size Distribution. *Fuel Process. Technol.* **2017**, *156*, 27−32.
(41) Muralidharan, G.; Runkana, V. Rheological Modeling of Spherical Polymeric Gels and Dispersions Incorporating the Influence of Particle Size Distribution and Surface Forces. *Ind. Eng. Chem. Res.* **2009**, *48*, 8805−8811.
(42) Cepuritis, R.; Jacobsen, S.; Pedersen, B.; Mørtsell, E. Crushed Sand in Concrete - Effect of Particle Shape in Different Fractions and Filler Properties on Rheology. *Cem. Concr. Compos.* **2016**, *71*, 26−41.

https://doi.org/10.1021/acsomega.2c03283
ACS Omega 2022, 7, 28493−28502